Journal of
Materials Chemistry A

Accepted Manuscript

Highly Efficient Visible-Light Driven Photocatalysts: A Case on Zinc Stannate Based Nanocrystal Assemblies

Cai-Hong Liu,[1] Robert Röder,[2] Lichun Zhang,[1] Zheng Ren,[1] Haiyan Chen,[3] Zhonghua Zhang,[1] Carsten Ronning,[2] and Pu-Xian Gao,[1,*]

[1]Department of Materials Science and Engineering & Institute of Materials Science, University of Connecticut, Storrs, Connecticut 06269-3136, USA, [2]Friedrich-Schiller-Universität Jena, Institut für Festkörperphysik, Max-Wien-Platz 1, D-07743 Jena, Germany, [3]Mineral Physics Institute, Stony Brook University, Stony Brook, New York, 11794, USA

* Corresponding author E-mail: puxian.gao@ims.uconn.edu

Keywords: zinc stannate, solar-light driven photocatalysis, hydroxyl radical, defects, hetero-epitaxial interface

Abstract

The design and discovery of green and highly efficient visible-light driven catalysts hold significant importance towards efficient harvesting, conversion and utilization of the full-spectrum solar energy. Here in this work, we report several wide band gap (> 3.1 eV) semiconducting nanostructures counterintuitively showing excellent catalytic activity under solar light towards organic dye degradation. These nanostructured stannates include amorphous $ZnSnO_3$ nanocubes and Zn_2SnO_4-SnO_2 nanocrystal assemblies, which possess the merits of high activity, low cost, absence of toxicity, and ease of synthesis. Hydroxyl radicals (·OH) are confirmed to be the major active species responsible for the dye degradation reactions. The catalysis tests under monochromatic light and optical characterizations revealed remarkable activities under the visible light range due to populated defect states in these semiconductor nanostructures. Finally, the Zn_2SnO_4-SnO_2 hetero-junction nanocrystal assemblies produced by slow-ramping thermal decomposition demonstrated very high photocatalytic efficiency under visible light, with dye molecules almost fully degraded in 20 min. Besides more visible-light-active defect states and larger crystallite size, the coherent (hetero-epitaxial) interfaces and strong type II heterojunction interaction between the spinel Zn_2SnO_4 and rutile SnO_2 nano-grains might be the main reasons for the drastically improved photocatalytic performance in the slow-ramp Zn_2SnO_4-SnO_2.

1. Introduction

Environmental remediation particularly in water treatment, disinfection and air purification are vital research issues toward sustainable ecosystem and environment. Since the early study of the photocatalytic oxidation of organic compounds in aqueous systems by Carey in 1976,[1] extensive investigations have been conducted on the photocatalytic decomposition of hazardous wastes into harmless chemicals.[2-4] In particular, the efficient utilization of full-spectrum solar energy in this regard has been pursued intensively. For example, visible-light or solar-light active catalysts for waste water purification and hydrogen generation demonstrate their unique merits in greenness, low-cost, and sustainability. The visible-light active TiO_2 based nanostructures have been intensively studied, mainly through alloying of either transition-metal cations or anions into TiO_2[5, 6] in order to tune its band gap into visible-light region. As a new class of photocatalysts, ternary or quaternary oxide based alternatives containing bismuth or vanadium have been found to be efficient for organic molecule decomposition under visible light illumination, such as $NaBiO_3$,[7] $Bi_2Mo_xO_y$,[8-11] $Bi_2Mo_xW_{1-x}O_6$,[12] $BiVO_4$,[13-15] $Ca_2Bi_2O_4$,[16] Bi_2WO_6,[7] $SnNb_2O_6$.[17, 18] The downsides of these Bi and V contained compounds are their high toxicity and relatively high cost due to the limited availability of these elements. Therefore, two issues arose from here. First, the search and design of efficient, green, and low-cost visible-light active photocatalysts are highly demanded. Secondly, most visible-light active photocatalysts require small band-gap to enable highly efficient visible-light absorption. It remains counterintuitive to expect a high catalytic efficiency under solar light for wide band-gap semiconductors, although defect induced visible light trapping may help enhance the absorption efficiency.[19] On the other hand, the impacts of defects on visible photocatalytic activity were rarely investigated.[20] Hence, the full understanding of the work principles is necessary to guide the material design and screening to fully utilize the sun light.

Here, several green and low-cost zinc stannate nanomaterial photocatalysts have been found to be highly efficient under visible continuous light and monochromatic light towards degradation of rhodamine B (RB) for the first time, including amphous mesoporous $ZnSnO_3$ nanocubes and Zn_2SnO_4-SnO_2 nanocrystal assemblies. Although these stannate semiconductors have wide band gaps, they possess radiative defect states in a broad visible region, which imply that the defect tuning can be as effective as band gap tuning towards utilizing solar energy. Hydroxyl radicals (·OH) were confirmed to be the key active oxidizers in the degradation reaction. By utilizing the rational thermal engineering of zinc stannate, Zn_2SnO_4-SnO_2 nanocrystal assemblies with controlled crystallite size and defect states were

obtained via a slow ramping process. Excellent photocatalytic performance under solar light was achieved. The hetero-epitaxial interfaces and stronger interactions between Zn_2SnO_4 and SnO_2 in the slow-ramp Zn_2SnO_4-SnO_2 sample are found to greatly enhance the photocatalytic activity as a result of promoted charge transfer efficiency.

2. Experimental Section

Materials Preparation: The precursor - porous zinc hydroxystannate $ZnSn(OH)_6$ (ZHS) nanocubes have been synthesized via a simple ionic substitution solution reaction at room temperature according to the method reported in literature.[21] By annealing these ZHS mesoporous nanocubes at 350 °C and 850 °C for 9 hours, respectively, $ZnSnO_3$ (ZS) and Zn_2SnO_4-SnO_2 (DZS-SnO_2) nanoparticles were obtained. The ramping rate is generally controlled at 20 °C/min.

Materials Characterization: The crystal structure of the synthesized samples was investigated by x-ray diffraction (XRD). The XRD measurements were conducted at room temperature using a Bruker AXS D8 ADVANCE diffractometer (Cu Kα radiation, λ=1.541 Å). The accelerating voltage, emission current, and scanning speed were set to 40 kV, 40 mA, and 5 degree.min^{-1}, respectively. Thermogravimetric analysis (TGA) and differential scanning calorimeter (DSC) were carried out using the TA Instruments Q600 in a nitrogen atmosphere with ceramic sample pans. The data were collected with a scan rate of 5 °C.min^{-1} over a temperature range of 0-1000 °C. The composition, structure and morphology of the stannate nanoparticles were further characterized using electron microscopies, such as scanning electron microscopes (JEOL 6335F FE-SEM and FEI Quanta FESEM) and a scanning transmission electron microscope (STEM, FEI Tecnai-12), both equipped with energy dispersive x-ray spectrometers (EDXs). A JEOL 2010 High resolution TEM (HRTEM) was used to acquire atomistic lattice images of various stannate nanostructures.

Varian Cary 5000 and Perkin Elmer 900 ultraviolet-visible-near-infrared (UV-vis-NIR) spectrophotometers were used for optical absorption measurements. Room temperature micro-photoluminescence (μPL) measurements were carried out using a HeCd continuous wavelength (CW) laser with an excitation wavelength of 325 nm in order to investigate the optical properties of the fabricated stannate nanostructures. The nanoparticle samples were deposited onto a clean Si substrate by a dry imprint technique. The laser was focused onto the sample with a spot size of ~ 18 μm² by a reflective objective (36x, NA = 0.5). The luminescence was collected by the same objective, dispersed by the 500 mm monochromator and detected by a nitrogen cooled charge-coupled device (CCD). XPS experiments were

performed on a scanning Auger Multi Probe PHI Spectrometer (Model 25-120) equipped with an Al source (1486.6 eV) at 200 W. The signal was filtered with a hemispherical analyzer. All the binding energies were calibrated to the C 1s peak at 284.6 eV of the surface adventitious carbon.

The specific surface areas were determined by the Brunauer-Emmett-Teller (BET) nitrogen adsorption and desorption method using a Micromeritics ASAP 2020 physi-sorption analyzer. The pore size distributions were calculated using the Barret-Joyner-Halenda (BJH) model based on nitrogen desorption isotherms.

Photocatalytic Studies: In a typical experiment, ca. 20 mg stannate nanoparticles were dispersed in a vial containing 20 mL of aqueous Rhodamine B (RB). Prior to illumination, the mixture was sonicated in dark for 15 min to establish the adsorption/desorption equilibrium. The suspensions were then centrifuged. The UV/VIS spectrum of the supernatant was taken as reference of the RB solution before photocatalysis test (0 min = C_0). Afterwards, the suspension was irradiated with a 22 W UV ring lamp (Luzchem, USA) owing an emission peaked at 365 nm. Degradation was monitored by analyzing aliquots withdrawn from the suspension at various illumination time intervals. The aliquot samples containing the photocatalyst and RB were centrifuged, and the absorption spectra of the supernatant solutions were recorded in a spectral range of 400-700 nm. The RB concentrations were determined using the Beer-Lambert law $A = \alpha c \ell$, where A is the maximum RB absorbance at 557 nm, α is the RB molar absorptivity, and ℓ is the sample cell length (1 cm). RB degradation was expressed as C/C_0 versus UV-illumination time, where C_0 is the initial concentration.

The photocatalyst ($ZnSnO_3$, Zn_2SnO_4-SnO_2, TiO_2) powders were directly dispersed in 20 mL of ca. 6.8×10^{-3} $g.L^{-1}$ RB aqueous solution with a concentration of ca. 1.0 $g.L^{-1}$. And the absorber/solution thickness was kept to be about 2.5 cm. A 150-W solar simulator (Model: 96000, Newport optics) with an Air Mass (AM) 1.5 global filter was used as a light source (beam diameter: 5 cm). The average light intensity striking on the reaction solution surface was ~ 300 $mW.cm^{-2}$. For the monochromatic light test, the above light beam was passed through various bandpass filters (λ =300, 420, 470, 550 nm, band width ~ 10 nm, beam diameter: 2.5 cm). The monochromatic light intensity was measured by an optical power meter (Model: 842-PE, Newport optics) combined with a thermopile sensor (Model: 818P-040-25, Newport optics). All monochromatic beams had an identical power density of ~ 7 $mW.cm^{-2}$.

The formation rate of ·OH at photo-illuminated sample/water interface was detected by PL spectroscopy using coumarin (COU) as a probe molecule. COU can readily react with ·OH and produce the highly fluorescent product 7-hydroxycoumarin (7HC). Experimental procedures were as follows: at ambient temperature, 0.1 g of catalyst powder sample was dispersed in 20 mL of 1 mmol.L^{-1} COU aqueous solution (absorber/solution thickness: ~ 1cm). The suspension was allowed to reach an adsorption–desorption equilibrium among the photocatalyst, COU, and water before illumination by sonication in dark for ~20 minutes. Additional experimental results indicated that the absorbed COU and 7HC on various semiconductor photocatalysts was less than 10%. Then, the above mixtures were irradiated under solar light beam (beam condition has been described earlier). After solar simulator illumination for every 10 or 20 min, the reaction solution was processed to measure the PL intensity by a Horiba Jobin-Yvon Spex Fluorolog-3 fluorimeter. The excitation wavelength was 344 nm and the scanning speed was 100 nm.min^{-1}. The width of emission slit was set to be 2.5 nm.

3. Results and Discussion

In this work, as-synthesized ZHS nanoparticle powders were used as precursors to obtain different zinc stannate semiconductor nanoparticles through post-synthetic thermal annealing. DSC measurements of the as-synthesized ZHS nanoparticles (Figure 1a) exhibited two peaks at 204 °C and 712 °C as a result of a two-step thermal decomposition process. At the first step ZHS is dehydrated to $ZnSnO_3$ (ZS), and then further decomposed to Zn_2SnO_4(DZS)-SnO_2 nanocomposites at the second step.[22] The XRD spectra in Figure 1b confirm that after the thermal treatment, the perovskite ZHS (JCPDS 20-1455) decomposed into amorphous ZS nanocubes and spinel DZS (JCPDS 73-1725)-rutile SnO_2 (JCPDS 41-1445) nanocrystal assemblies after annealing at 350 °C and 850 °C, respectively. Figures 1c and 1d further confirm the amorphous structure of ZS with a stoichiometric Zn:Sn:O ratio of 1:1:3

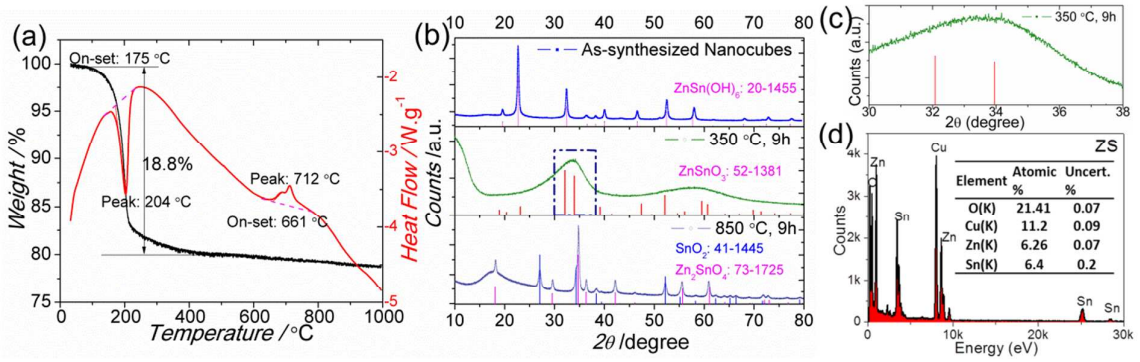

Figure 1. (a) Thermogravimetric analysis (TGA) and differential scanning calorimeter (DSC) diagrams of as-synthesized ZHS nanoparticles. (b) XRD patterns of as-synthesized ZHS, amorphous ZS and DZS-SnO_2 nanostructures after thermal annealing. The corresponding standard JCPDS cards are also included for ZHS (top) and DZS-SnO_2 (bottom) in the graph, with ilmenite-type $ZnSnO_3$ as a reference JCPDS card in the amorphous ZS spectrum (middle). (c) Zoom-in XRD pattern of amorphous ZS showing no obvious crystalline peaks. (d) Typical TEM energy dispersive X-ray spectrum (EDXS) of amorphous ZS, with Cu signal from TEM grid.

Figures 2a and 2b show the SEM and EM images of the as-synthesized ZHS mesoporous nanocube precursor. The TEM analysis (Figure 2b upper right inset) revealed the single crystalline and mesoporous nanocube structure with an average diameter of 37±8 nm (30-50 nm) and relatively smooth surfaces. The mesoporous nature of individual nanocubes after thermal treatment at 350 °C for 9h is clearly displayed in the brightness contrast shown in Figure 2c. The obtained amorphous structure in ZS was identified by the diffusive ring-like electron diffraction pattern in the inset of Figure 2c. In contrast, the obtained DZS-SnO_2 after higher temperature thermal treatment (850 °C) displayed a solid and crystalline structure with polyhedron and other irregular shapes (Figures 2c-d & S1). Their lattice images clearly revealed a spinel DZS structure (FCC, $Fd\bar{3}m$, a = 8.610 Å) with exactly matched lattice spacings to the {220}, {311}, and {131} lattice planes (Figure 2e) and a rutile SnO_2 tetragonal structure (P42/mnm, a = 4.738 Å, c = 3.187 Å) with {110}, {011}, and {101} lattice planes identified (Figure 2f). The specific surface area and inner pore size evolution of zinc stannate after thermal treatment was shown in the supplementary information(Figure S1 and Table S1), which further reflected the above morphology/structure evolution analysis).

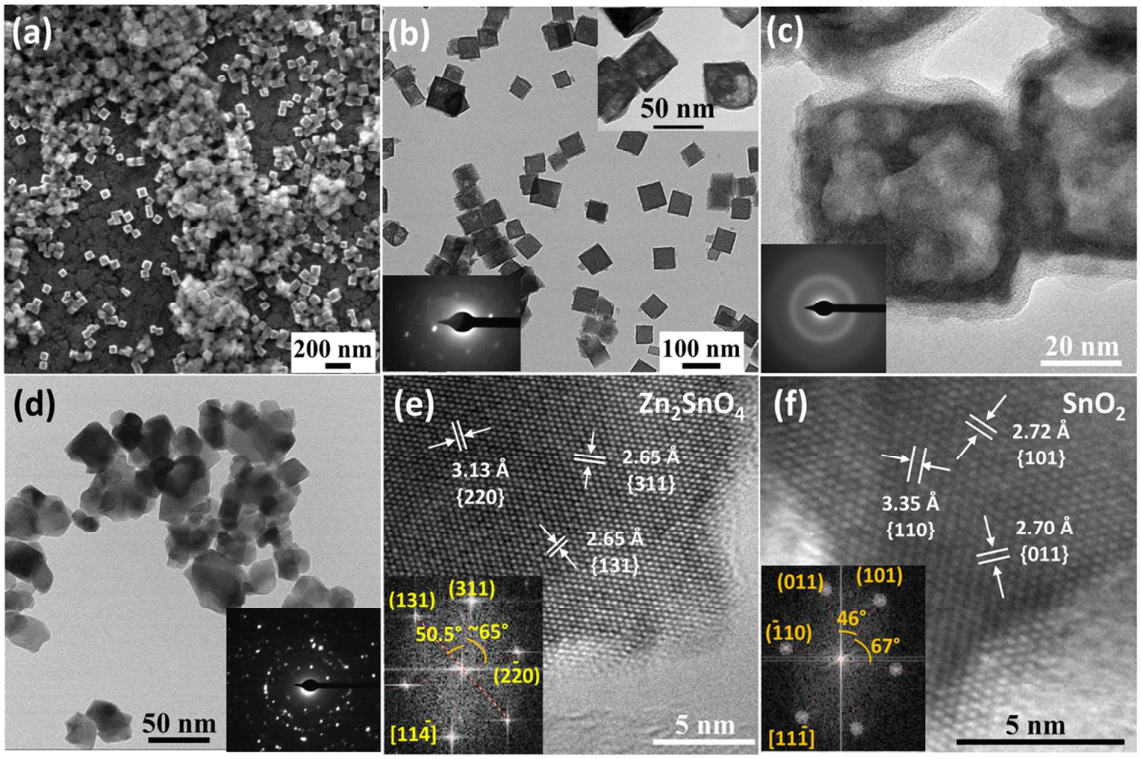

Figure 2. Electron microscopy analysis on structure and morphologies of zinc stannate based nanoparticles. (a) SEM and (b) TEM images of ZHS mesoporous nanocube precursor, TEM image of (c) $ZnSnO_3$ porous nanoparticle and (d-f) Zn_2SnO_4-SnO_2 via thermal decomposition of ZHS precursors. (e) and (f) are HRTEM images of Zn_2SnO_4 and SnO_2 nanocrystals in Zn_2SnO_4-SnO_2 composite. The insets in (b-d) and (e-f) are SAED and fast Fourier transform (FFT) images, respectively.

The band gaps of zinc stannate based semiconductors have reported values ranging from 3.2 eV to 4.1 eV,[23, 24] similar as SnO_2.[25-27] Hence, firstly, photodegradation of Rhodamine-B (RB) dye molecules was studied upon stannate nanostructures' exposure to UV light centered at λ = 365 nm in comparison with commercial TiO_2 (Figures 3a-c). The degradation of RB under UV light also was tested as a blank sample for comparison. Only 5% and 30% of RB contents were left after 2h illumination in the presence of ZS and DZS-SnO_2, respectively. However, RB was fully decomposed after only half an hour of UV illumination in the presence of the same amount of TiO_2 nanoparticles. In order to quantitatively compare their photocatalytic activity, reaction kinetics were analyzed based on the UV-vis-NIR absorption spectroscopy data in Figure 3. Most of the photo-degradation reactions of organic molecules obey the first order reaction kinetics,[28-30] where the relationship between degradation rate and illuination time t can be described by $\ln (C/C_0) = -k \cdot t$. Here, k is the degradation rate constant, C_0 is the

initial concentration, and *C* represents the RB concentration after an illumination time of *t*. Figure 3d shows the $\ln(C/C_0)$ versus illumination time plots for the three photocatalysts examined. The first order linear regression was fitted and used to determine the reaction rate constant k, which increased from 1.80×10^{-4} min^{-1} in blank sample to 9.5×10^{-3}, 0.028, and 0.15 min^{-1} in presence of DZS-SnO_2, ZS, and TiO_2 nanoparticle in solutions, respectively.

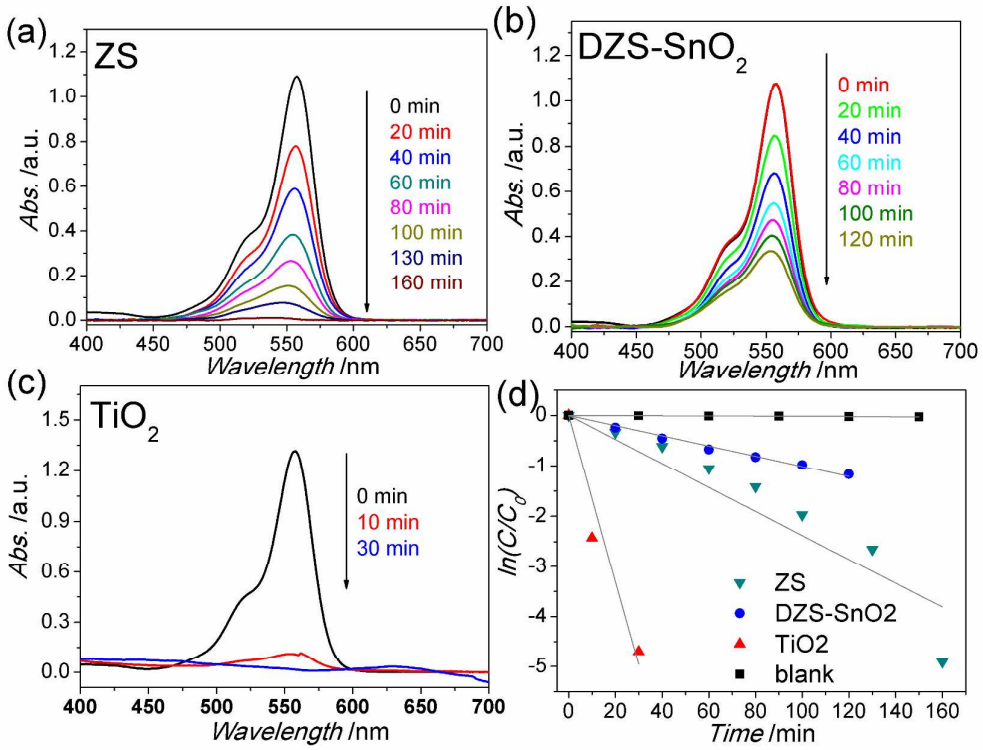

Figure 3. Absorption spectra in RB solution during illumiation of UV light (λ = 365 nm) in the presence of nanoparticles of (a) amorphous ZS nanocubes, (b) Zn_2SnO_4(DZS)-SnO_2 nanocrystal assemblies, and (c) P25 TiO_2 nanoparticles. (d) First-order reaction kinetic plots for photocatalytic degradation of RB solution with or without (blank) the above photocatalysts. The initial RB concentration was C_0 = 5 $mg.L^{-1}$, while C represents the RB concentration as a function of illumination time *t*.

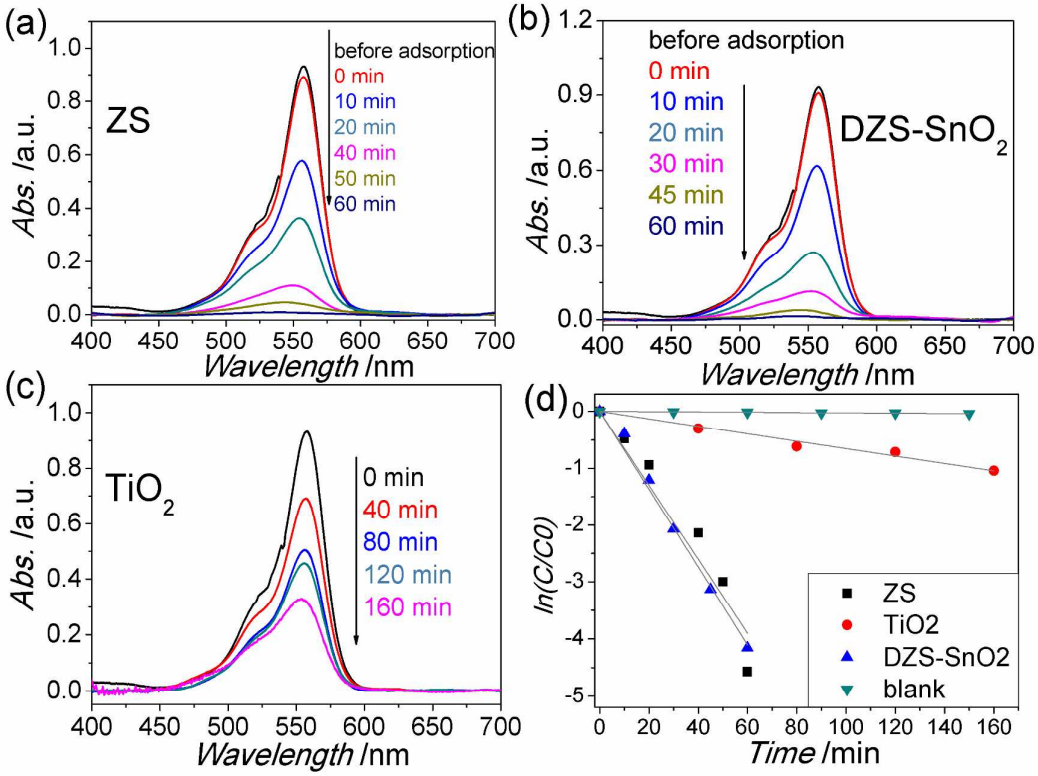

Figure 4. Absorption spectra of RB solution under solar-simulator illumination in the presence of nanoparticles of (a) amorphous ZS nanocubes, (b) DZS-SnO_2 nanocrystal assemblies, (c) P25 TiO_2 nanoparticles, and (d) the first-order reaction kinetics plot for degradation of RB solution with and without above photocatalysts.

When the photocatalytic measurements were performed under a solar simulator, which mainly contains visible light (~ 44% of the sun's energy), the results were quite fascinating and are illustrated in Figure 4. RB was fully degraded after 1 hour using ZS and DZS-SnO_2 as photocatalysts, demonstrating a much higher activity under solar-simulator light than under monochromatic UV light. Instead, over 40% of RB was intact even after 2 hour in the presence of the same amount of TiO_2 P25 photocatalysts. From the fitting of the data in Figure 4d, the reaction rate constants were calculated to be 0.0712, 0.0721, 6.25×10^{-3} min^{-1}, and 2.50×10^{-4} min^{-1} for ZS, DZS-SnO_2, TiO_2, and no photocatalyst (blank), respectively. The photo-degradation reaction occurs in ZS and DZS-SnO_2 10 times faster than in existence of the same amount of TiO_2 nanoparticles under solar-simulator illumination.

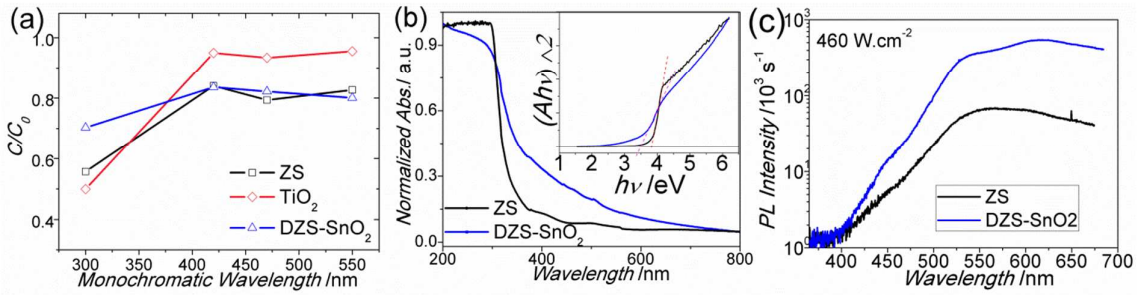

Figure 5. (a) Wavelength dependence of RB decomposition in the presence of different photocatalysts upon illumination of monochromatic lights with various wavelengths (300, 420, 470, 550 ± 5 nm) for 30 min. These monochromatic lights generated using different bandpass filters have nearly identical intensities (~7 mW.cm^{-2}). (b) Absorption spectra and (c) photoluminescence spectra of amorphous ZS (black) and DZS-SnO_2 nanocrystal assemblies (blue). The inset in Figure 5b is used for extracting optical band gaps of these zinc stannate based nanoparticles. The PL spectra of ZS and DZS-SnO_2 ensembles were excited using a 325 nm HeCd laser with a beam power of 460 W.cm^{-2}.

To gain further understanding of the photocatalytic properties provided by these stannate nanostructures, their wavelength-dependent activity towards photodegradation of RB was measured. Therefore, four monochromatic illuminations were selected using bandpass filters, with the results shown in Figure 5a. The intensity of each illumination was ~ 7 mW.cm^{-2}, only about 1/75 of the intensity of the full-spectrum beam generated by a solar simulator. It can be seen that the P25 TiO_2 nanoparticles show higher efficiency than ZS and DZS-SnO_2 nanoparticles in the UV range with the best performance shown under 300 nm light. However, both ZS and DZS-SnO_2 reveal much better activities than TiO_2 in the visible range up to 550 nm. After exposure for 30 minutes under 420, 470, and 550 nm illumination, nearly no RB was degraded within the TiO_2 suspension, while over 20% of RB was converted in both stannate suspensions for $\lambda > 400$ nm. These results are consistent with the previous results shown in Figures 3 and 4.

The optical and electronic properties of these nanoparticles have been investigated using optical absorption and photoluminescence (PL) spectroscopies shown in Figures 5b and 5c. Despite the strongest absorption of ZS and DZS-SnO_2 films being in the UV region, significant absorbance is still observed in the visible range of 400 - 800 nm, especially for DZS-SnO_2, possibly indicating a high defect concentration. While the comparative TiO_2 nanoparticle sample also showed some extent of visible range absorption (Figure S2), which

might be due to the diffusive scattering effect. Their optical band gaps can be extracted from the Tauc plot in Figure 5b inset with E_g values of about 3.84 eV and 3.33 eV for amorphous ZS nanocubes and DZS-SnO_2 nanocrystal assemblies, respectively. It is noted here that the Eg value for DZS-SnO_2 is extracted based on the composite absorption spectrum from both DZS and SnO_2 nancrystals for simplification purpose. Meanwhile, broad PL peaks were observed in the visible region without significant UV peaks which could be related to the intrinsic band gap emission for both ZS and DZS-SnO_2. Two main PL peaks were identified in the ZS sample, centered around ~ 555 nm and ~ 615 nm. Even stronger emission bands were revealed corresponding to defect states in DZS-SnO_2, as shown in Figure 5c. These emissions could be caused by oxygen vacancies, Zn interstitials, etc.[31, 32]. Such defect levels in the band structures of ZS and DZS-SnO_2 may contribute significantly to their highly efficient visible-light driven photocatalytic performance.

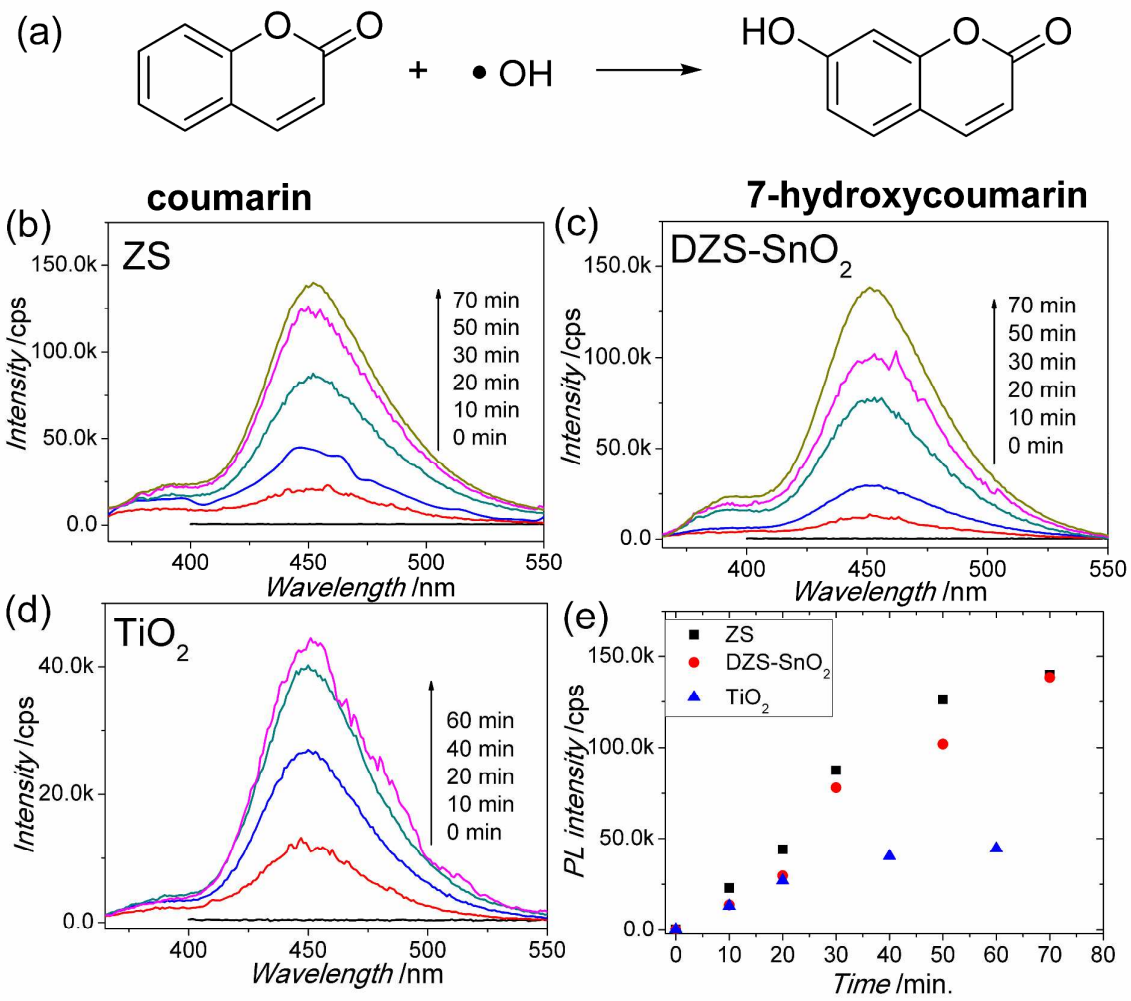

Figure 6. (a) Formation of 7-hydroxycoumarin (7HC) by the reaction between ·OH and coumarin (COU).[33] Photoluminescence spectra of COU-photocatalyst suspension after solar-simulator illumination of (b) amorphous ZS, (c) DZS-SnO_2 nanocrystal assemblies, and (d) commercial P25 TiO_2 nanoparticles. (e) PL intensity as a function of solar-simulator illumination time. The COU initial concentration was 1 mmol.L^{-1}.

According to traditional photocatalytic theory, the oxidation reaction of the dye is generally believed to be initiated by ·OH and $\cdot O_2^-$ radicals.[3, 4, 34, 35] The formation of $\cdot O_2^-$ and ·OH can be detected by electron spin resonance (ESR) and photoluminescence since these two radicals can be captured by either a magnetic field or some fluorescent probe molecules, such as 2-chloro-1,3-dibenzothiazolinecyclohexene[36] and 4′,9′-Bis(diphenylphosphinyl) naphthofluorescein[37] for O_2^-·, terephthalic acid[38, 39] and coumarin (COU)[40, 41] for ·OH.

In this work, the generation of ·OH on photocatalysts ZS and DZS-SnO_2 was investigated using photoluminescence measurements with COU, which is supposed readily to react with ·OH in photo-illuminated sample/water interface to produce the highly fluorescent product, 7HC (shown in Figure 6a) with a PL signal at 456 nm. Figures 6b-d show the PL spectra evolution from 1 mmol.L^{-1} COU solution under solar simulator illumination as a function of time in the presence of ZS, DZS-SnO_2, and TiO_2 nanoparticles. There is no signal of 7HC (or ·OH) before illumination, and then a gradual and proportional augment in the PL intensity at about 456 nm occurring with increasing illumination time. High intensities of the 7HC signal (or ·OH) were detected after 1 hour in both ZS and DZS-SnO_2 suspensions, which were around three times more intense than that in the TiO_2 suspension after 1 hour. Figure 6d shows that the formation rates of ·OH in the presence of ZS and DZS-SnO_2 were almost same and kept constant while that of ·OH in the TiO_2 system was much lower and largely decreased after 50 min. These results are consistent with their photocatalysis performance under solar light, proving that both ZS and DZS-SnO_2 nanoparticles are highly efficient photocatalysts due to the efficient generation of ·OH. It is worth noting that only a portion of the ·OHs were detected and the formation rate or concentration of ·OH is actually underestimated due to the short lifetime and relatively low diffusion rate of ·OH, which leads to a low detection efficiency.[40]

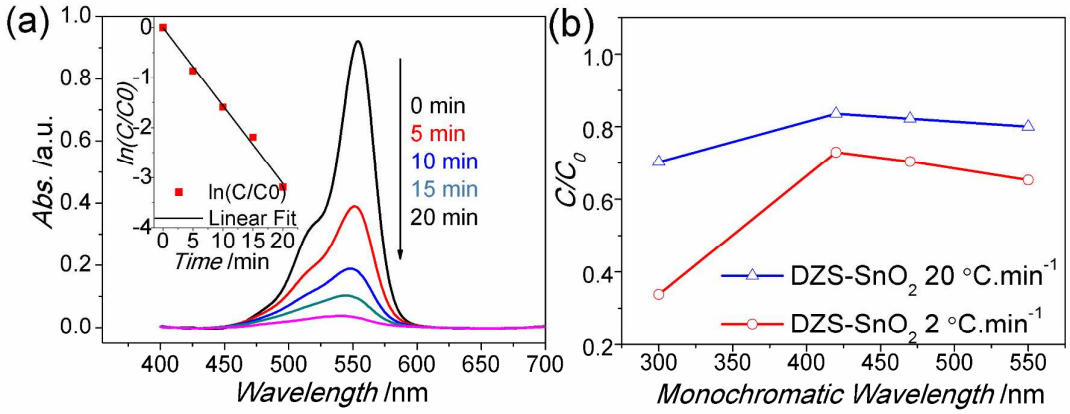

Figure 7. Photocatalytic behavior of DZS-SnO_2 nanocrystal assemblies obtained by the slow-ramp annealing (2 °C.min^{-1}, 850 °C, 9h). (a) RB absorption spectrum evolution and kinetics plot for degradation rate constant (inset) under solar-simulator illumination, (b) monochromatic light wavelength dependence of RB degradation after illumination for 30 min.

Defects, upon tuned properly, can benefit or hamper the catalytic performance through either trapping carriers/radicals or functioning as active sites. In this work, the populated visible defect energy states have been confirmed to be responsible for their visible-light driven catalytic activities. Considering the tunability of defect states and concentration, controllability of crystallinity, and possible heterojunction induced synergistic effect,[6, 42-44] DZS-SnO_2 composite has been chosen for further exploration of their photocatalytic behavior. As a control strategy, post thermal treatment was found to enable further controlled DZS-SnO_2 composites with tunable catalytic performance. For example, a much slower ramping rate (2 °C.min^{-1}) during the thermal annealing was used to compare it with the previously used one (20 °C.min^{-1}). The temperature history profiles are illustrated in the supporting information (Figure S3). The photocatalytic behaviors were then investigated under the same conditions using a solar simulator. Surprisingly, the RB was almost completely decomposed after only 20 minutes, instead of 60 minutes in the fast heating sample mentioned above. The photodegradation efficiency of slow-ramping samples is four times that of the DZS-SnO_2 nanoparticles obtained after a fast ramping (20 °C.min^{-1}) thermal treatment. The kinetic analysis in Figure 7a inset shows the perfect first order reaction characteristic. The decomposition rate constant was calculated to be ~0.154 min^{-1}, about 25 times that of TiO_2 nanopowders (6.25×10^{-3} min^{-1}) and even better than that of TiO_2 under UV illumination (0.150 min^{-1}). Notably, this is an extremely high efficiency under solar-light illumination compared to various literature reported numbers.[7-9, 12, 17] Coincidently, the wavelength-

dependent efficiency towards RB degradation (Figure 7b) is also much higher with slow-ramp DZS-SnO_2 samples under all wavelengths than that with fast-ramp treated one.

To reveal and understand the mechanisms for the improved catalytic activity in slow-ramping thermally treated samples, further structural and optical characterizations were carried out including TEM, HRTEM, XRD, PL, and X-ray photoelectron spectroscopy (XPS). Figures 8a and 8b show HRTEM images for these two DZS-SnO_2 samples, in which the DZS and SnO_2 domains have been marked. Based on this HRTEM data analysis, the crystallite sizes of SnO_2 and DZS using the slow-ramp heating are around 10-25 nm and 15-35 nm, respectively. Both components in fast-ramp composite have much smaller crystallite size, which are around 5-15 nm and 10-20 nm for SnO_2 and DZS, respectively. Similar results on crystallite size have also been obtained from XRD and shown in Figure S4 and data were summarized in Table S2. There is no obvious difference in particle size and their polyhedral or irregular morphologies of these two DZS-SnO_2 nanocrystal assemblies. In the heterogeneous catalyst system, larger crystallite sizes can suppress the charge recombination or trapping either at the interface or in the crystal domains of two semiconductor phases.[3, 30] This could be one of the main reasons for the improved photocatalytic activity in the slow-ramp produced DZS-SnO_2.

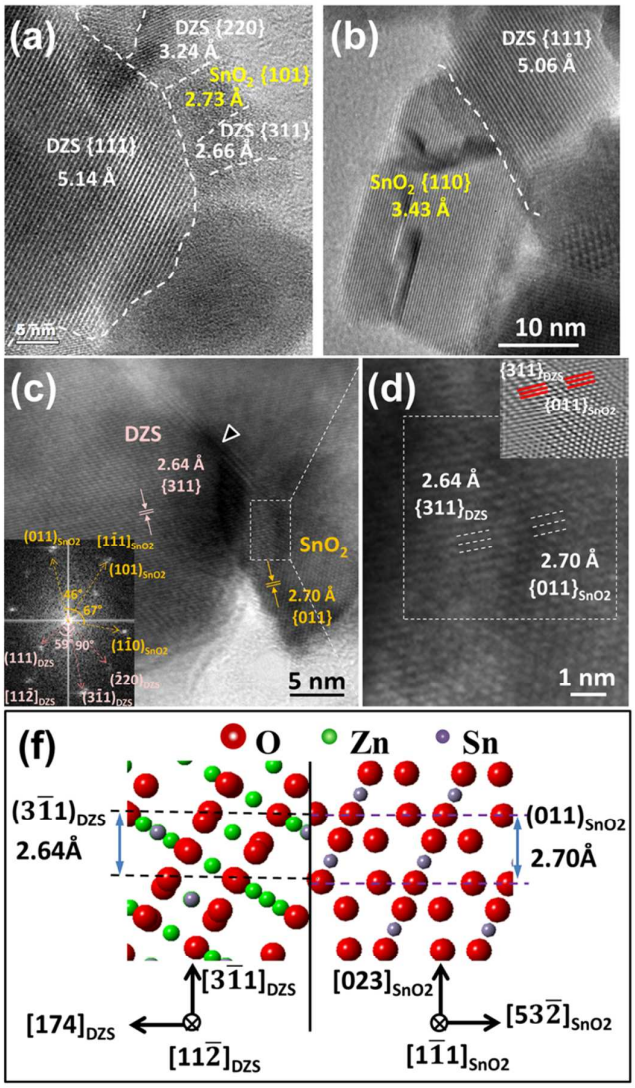

Figure 8. High resolution TEM images for DZS-SnO_2 nanocrystal assemblies obtained under different annealing conditions: (a) slow ramping 2 °C.min^{-1}; (b) fast ramping 20 °C.min^{-1}. (c-d) HRTEM images of coherent interfaces of multiple adjacent nanocrystals in the slow-ramp sample. (f) Schematic models of the coherent atomic arrangements between (011) SnO_2 planes and (3$\bar{1}$1) DZS planes. Insets in (c) and (d) are FFT and inverse FFT images, respectively.

In HRTEM investigations, different phase separation scenarios have been observed involving individual domains and the interfaces of DZS and SnO_2. Figures 8c and 8d illustrate the phase separation of DZS and SnO_2 in slow-ramp DZS-SnO_2 composites. DZS and SnO_2 domains have been identified and a typical heteroepitaxial interface between DZS and SnO_2 was observed. The fast-Fourier transform (FFT) pattern (Figure 8c, insert) revealed two sets of diffraction patterns corresponding to the spinel cubic DZS [11$\bar{2}$] zone axis pattern and rutile

tetragonal SnO_2 [$1\bar{1}1$] zone axis pattern. The coherent interface forms between $(011)_{SnO2}$ and $(3\bar{1}1)_{DZS}$, whose interplanar spacings are measured to be 0.270 nm and 0.264 nm from the FFT pattern, with a 2.27% lattice mismatch. As a result, structural defects such as misfit dislocations are formed in either DZS or SnO_2 phase domains in order to release the coherent interface stress. In the present case, misfit dislocations were marked by a white triangle arrow in the Figure 8c. It is worth noting that the above epitaxial interfaces are populated in the slow-ramp DZS-SnO_2 samples. While there was no lattice alignment observed in the fast-ramp DZS-SnO_2 samples. It is known that the charge transport across coherent interfaces with small lattice mismatch is generally more efficient than incoherent interfaces due to the sharper band structure alignment with lower electronic energy barrier height.[45-48] Hence, this populated epitaxial interfaces between DZS and SnO_2 nanocrystals generated during a slow annealing process could contribute to the enhancement of their photocatalytic activity. It is reasonable that in a slow annealing process, the interface energy can reach the lowest state via an orientation adjustment in a given long period of time, which is however, much harder in a fast ramping process.

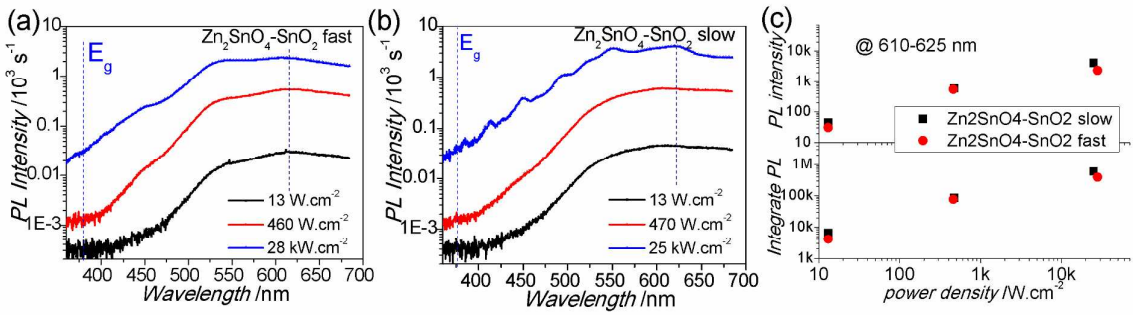

Figure 9. Photoluminescence (PL) spectra of DZS-SnO_2 nanocrystal assembly by (a) fast-ramp and (b) slow-ramp treatment uponexcitation by a 325 nm HeCd laser with various power densities. The spectra were normalized to the measuring time. (c) Plots of the PL intensity evolution under different excitation power density, including individual PL band at ~ 610 – 625 nm (up) and integrated PL in the whole range (bottom).

The PL spectra collected under variable excitation power densities shown in Figure 9 were used to investigate the defect states and carrier killer center concentration in DZS-SnO_2 fast-ramp and slow-ramp samples. Both crystal DZS-SnO_2 samples show strong, defect driven PL emission in the green and red visible light region between 500 nm and 700 nm while with slightly higher luminescence intensity for the slow-ramp crystals under all excitations, indicating a higher concentration of radiative defects. Moreover, the PL of slow-ramp DZS-SnO_2 kept more proportional increase with excitation power density (for the PL emission band

at ~ 615 nm as well as for the integrated PL, as shown in Figure 9c) while the fast-ramp sample seems to reveal more obvious a saturation effect of the defect emission with lower PL under 25-28 kW.cm^{-2} excitation. The observed saturation effect in the yellow and red emission region is caused either by the smaller crystallite volume or by a higher number of killer centers in the fast ramp sample. Killer centers would lower the carrier lifetime, thus they might not contribute to photocatalysis. Meanwhile, the PL emission of the slow-ramp sample extends further into the blue spectral region with evolving blue emission bands, while this trend is weaker for the fast-ramp sample. Therefore, we obtain more optically active states over the visible spectral region (~380 - 700 nm) for the slow-ramp sample compared to the fast-ramp sample, thus they might contribute to photocatalysis. Therefore, the improved photocatalytic performance is likely caused by a superposition of the defect saturation in the fast-ramp sample and the increased number of optically active defect sates in the slow-ramp sample.

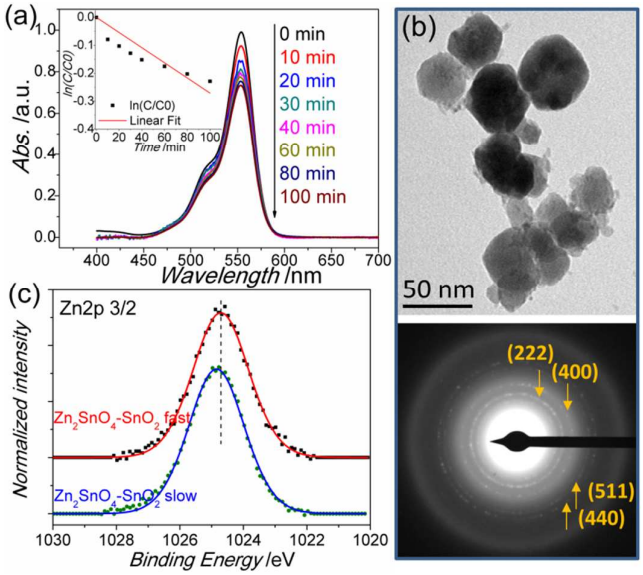

Figure 10. (a) Photocatalytic performance of DZS-SnO_2 physical mixture (2 °C.min^{-1}, 850 °C, 9h) towards RB degradation under solar simulator illumination. (b) TEM image and corresponding diffraction pattern of DZS nanoparticles after thermal treatment. (c) Zn 2p XPS spectra of DZS-SnO_2 nanocrystal assemblies obtained via fast- and slow-ramp (20 and 2 °C.min^{-1}, respectively) thermal treatments.

Our previous work has revealed that the interaction between two semiconductors in a heterogeneous catalysts system is vital for the photocatalytic performance under UV light.[42, 43] Recently, type II heterojunction photocatalysts were found with improved photocatalytic performance in organic pollutant degradation[6, 44] and solar water splitting.[49, 50] Through positive interactions between two semiconductors, the photon-excited electron-hole pair can

be separated efficiently with a longer life time. The effect of heterojunction interaction on the photocatalytic performance was investigated here. Firstly, the catalytic activity of the physical mixture of DZS and SnO_2 nanoparticles was tested for comparison (Figure 10a). The as-synthesized DZS and commercial SnO_2 were treated at 850 °C annealing with 2 °C.min^{-1} ramping rate before mixing and test (synthetic method and material basic characterizations shown in supporting information, Figure 10b, and Figure S5). A very low rate constant (3.19×10^{-3} min^{-1}, Table 1) under solar light was obtained from the physical mixture of DZS and SnO_2 nanoparticles. XPS analysis was further carried out (Figures 10c and S5) to compare the surface binding energy states and interaction between DZS and SnO_2. The O1s and Sn3d peaks are almost identical for fast- and slow-ramp DZS-SnO_2 (Figure S5 and Table S3). While, the Zn2p of DZS-SnO_2 slow-ramp showed a similar binding energy to that of DZS-SnO_2 fast-ramp sample, which are located at 1024.9 eV and 1024.7 eV for Zn 2p3/2, respectively. It has been reported that depending on the synthetic method, the Zn 2p3/2 signal of nano-sized Zn_2SnO_4 is normally located in a range of 1021.9 eV- 1024.5 eV.[51, 52] Our DZS-SnO_2 nanocomposites with Zn 2p peaks at even larger binding energies imply the stronger interaction induced electron shift between DZS and SnO_2. Based on above characterization results and discussions, the defect states, crystallite size, interface coherency, and heterojunction induced phase interactions are the main reasons for the excellent photocatalytic performance demonstrated in the DZS-SnO_2 slow-ramp samples.

Table 1. summary of the rate constant of photodegradation of RB in presence of various photocatalysts.

Degradation rate constant (min^{-1}) / Illumination condition	Blank	TiO_2	ZS (amorphous)	DZS-SnO_2 (fast-ramping)	DZS-SnO_2 (slow-ramping)	DZS-SnO_2 Physical mixture
UV ring lamp (22 W)	1.80×10^{-4}	**0.150**	0.028	9.50×10^{-3}	/	/
Solar simulator (300 mW.cm^{-2})	2.50×10^{-4}	6.25×10^{-3}	0.0712	0.0721	**0.154**	3.19×10^{-3}

4. Conclusion

$ZnSnO_3$ mesoporous nanocubes and Zn_2SnO_4-SnO_2 nanoparticles have been achieved by utilizing thermal engineering of zinc hydroxystannate nanocubes. Both of these large band gap (Eg > 3.1 eV) photocatalysts which possess radiative defect states in the broad visible region showed much better performance under solar simulator illuminations than under UV light (310 - 400 nm) towards dye degradation. It implies that defects tuning can be as effective

as band gap tuning towards utilizing solar energy. For the first time, zinc-based stannate nanostructures are reported as efficient visible-light driven photocatalysts. The monochromatic light analysis and optical property investigations indicate that the relative high activity of $ZnSnO_3$ and DZS-SnO_2 composites in the visible wavelength range was due to populated defect state induced transitions in the visible range. The DZS-SnO_2 nanocomposites' photocatalytic activity was dramatically affected by the annealing conditions. By decreasing the heating rate from 20 to 2 ºC.min^{-1}, DZS-SnO_2 composites with much more radiative defect energy levels and larger crystallite size was obtained and revealed a much higher activity under solar light illumination. Moreover, the populated epitaxial interfaces and strong heterojunction interaction between spinel DZS and rutile SnO_2 nano-grains were found during the slow phase separation and annealing process. In all, the larger grain size, more active defect levels, epitaxial phase separation, and strong interaction between DZS and SnO_2 in slow-ramp DZS-SnO_2 are considered to be the main reasons for its much higher photocatalytic activity than fast-ramp one under solar light illumination. These hetero-phase nanoparticle assemblies could be extended as promising catalysts for the efficient visible-light-driven fuel production and treatment of air pollution and waste water sources.

Supporting Information

BET surface area, pore distribution and morphology of ZHS, ZS nanocubes, and DZS-SnO_2 nanoparticles. UV-vis absorption spectrum of P25 TiO_2 nanoparticles. Temperature profiles for the fast and slow ramping treatment of samples. XRD patterns of DZS-SnO_2 fast- and slow-ramp samples. physico-chemical characterizations of DZS-SnO_2 physical mixture samples and XPS analysis of DZS-SnO_2 samples obtained after fast- and slow-ramp annealing.

Acknowledgements

The authors are grateful for the financial support from the University of Connecticut New Faculty start-up funds, the U.S. Department of Energy, the United Technologies Research Center, and the German DFG under the FOR1616 program.

References

1. J. Carey, J. Lawrence and H. Tosine, *Bull. Environ. Contam. Toxicol.*, 1976, **16**, 697-701.
2. H. Tong, S. Ouyang, Y. Bi, N. Umezawa, M. Oshikiri and J. Ye, *Adv. Mater.*, 2012, **24**, 229-251.
3. A. L. Linsebigler, G. Lu and J. T. Yates, *Chem. Rev.*, 1995, **95**, 735-758.
4. C. S. Turchi and D. F. Ollis, *J. Catal.*, 1990, **122**, 178-192.
5. M. Pelaez, N. T. Nolan, S. C. Pillai, M. K. Seery, P. Falaras, A. G. Kontos, P. S. M. Dunlop, J. W. J. Hamilton, J. A. Byrne, K. O'Shea, M. H. Entezari and D. D. Dionysiou, *Appl. Catal., B*, 2012, **125**, 331-349.

6. W. Zhao, W. Ma, C. Chen, J. Zhao and Z. Shuai, *J. Am. Chem. Soc.*, 2004, **126**, 4782-4783.
7. K. Yu, S. Yang, H. He, C. Sun, C. Gu and Y. Ju, *J. Phys. Chem. A*, 2009, **113**, 10024-10032.
8. A. Martínez-de la Cruz, S. Obregón Alfaro, E. López Cuéllar and U. Ortiz Méndez, *Catal. Today*, 2007, **129**, 194-199.
9. C. Belver, C. Adán and M. Fernández-García, *Catal. Today*, 2009, **143**, 274-281.
10. J. Bi, L. Wu, J. Li, Z. Li, X. Wang and X. Fu, *Acta Mater.*, 2007, **55**, 4699-4705.
11. A. Martínez-de la Cruz and S. Obregón Alfaro, *Solid State Sci.*, 2009, **11**, 829-835.
12. L. Zhou, M. Yu, J. Yang, Y. Wang and C. Yu, *J. Phys. Chem. C*, 2010, **114**, 18812-18818.
13. L. Ge, *J. Mol. Catal. A: Chem.*, 2008, **282**, 62-66.
14. F. Lin, D. Wang, Z. Jiang, Y. Ma, J. Li, R. Li and C. Li, *Energy Environ. Sci.*, 2012, **5**, 6400-6406.
15. N. C. Castillo, A. Heel, T. Graule and C. Pulgarin, *Appl. Catal., B*, 2010, **95**, 335-347.
16. J. Tang, Z. Zou and J. Ye, *Angew. Chem., Int. Ed.*, 2004, **43**, 4463-4466.
17. S. Liang, R. Liang, L. Wen, R. Yuan, L. Wu and X. Fu, *Appl. Catal., B*, 2012, **125**, 103-110.
18. S. Liang, S. Zhu, Y. Chen, W. Wu, X. Wang and L. Wu, *J. Mater. Chem.*, 2012, **22**, 2670-2678.
19. R. M. Sheetz, I. Ponomareva, E. Richter, A. N. Andriotis and M. Menon, *Phys. Rev. B*, 2009, **80**, 195314.
20. X. Pan, M.-Q. Yang, X. Fu, N. Zhang and Y.-J. Xu, *Nanoscale*, 2013, **5**, 3601-3614.
21. Z. Wang, J. Liu, F. Wang, S. Chen, H. Luo and X. Yu, *J. Phys. Chem. C*, 2010, **114**, 13577-13582.
22. P. Ramamurthy and E. A. Secco, *Can. J. Chem.*, 1971, **49**, 2813-2816.
23. M. A. Alpuche-Aviles and Y. Wu, *J. Am. Chem. Soc.*, 2009, **131**, 3216-3224.
24. H. Kou and S. Yang, *J. Phys. Chem. C*, 2012, **116**, 6376-6382.
25. J. Zhao, X. J. Zhao, J. M. Ni and H. Z. Tao, *Acta Materialia*, 2010, **58**, 6243-6248.
26. P. Tiwana, P. Docampo, M. B. Johnston, L. M. Herz and H. J. Snaith, *Energy & Environmental Science*, 2012, **5**, 9566-9573.
27. Z. Chen, J. K. L. Lai, C. H. Shek and H. Chen, *Journal of Materials Research*, 2003, **18**, 1289-1292.
28. J. Lin, J. Lin and Y. Zhu, *Inorg. Chem.*, 2007, **46**, 8372-8378.
29. C. Ye, Y. Bando, G. Shen and D. Golberg, *J. Phys. Chem. B*, 2006, **110**, 15146-15151.
30. J. B. Joo, Q. Zhang, M. Dahl, I. Lee, J. Goebl, F. Zaera and Y. Yin, *Energy Environ. Sci.*, 2012, **5**, 6321-6327.
31. H.-F. Lin, S.-C. Liao, S.-W. Hung and C.-T. Hu, *Mater. Chem. Phys.*, 2009, **117**, 9-13.
32. K. R. G. Karthik, B. P. Andreasson, C. Sun, S. S. Pramana, B. Varghese, C. H. Sow, N. Mathews, L. H. Wong and S. G. Mhaisalkar, *Electrochem. Solid-State Lett.*, 2011, **14**, K5-K7.
33. G. Louit, S. Foley, J. Cabillic, H. Coffigny, F. Taran, A. Valleix, J. P. Renault and S. Pin, *Radiat. Phys. Chem.*, 2005, **72**, 119-124.
34. W. Du, D. Deng, Z. Han, W. Xiao, C. Bian and X. Qian, *CrystEngComm*, 2011, **13**, 2071-2076.
35. W. Wang, L. Zhang, T. An, G. Li, H.-Y. Yip and P.-K. Wong, *Appl. Catal., B*, 2011, **108–109**, 108-116.
36. J. J. Gao, K. H. Xu, B. Tang, L. L. Yin, G. W. Yang and L. G. An, *FEBS J.*, 2007, **274**, 1725-1733.
37. K. Xu, X. Liu and B. Tang, *ChemBioChem*, 2007, **8**, 453-458.
38. X. Yu, J. Yu, B. Cheng and B. Huang, *Chem.--Eur. J.*, 2009, **15**, 6731-6739.

39. H. Dong, Z. Li, X. Xu, Z. Ding, L. Wu, X. Wang and X. Fu, *Appl. Catal., B*, 2009, **89**, 551-556.
40. Q. Xiang, J. Yu and P. K. Wong, *J. Colloid Interf. Sci.*, 2011, **357**, 163-167.
41. H. Czili and A. Horváth, *Appl. Catal., B*, 2008, **81**, 295-302.
42. Z. Zhang, H. Gao, W. Cai, C. Liu, Y. Guo and P.-X. Gao, *J. Mater. Chem.*, 2012, **22**, 23098-23105.
43. D. Jian, P.-X. Gao, W. Cai, B. S. Allimi, S. Pamir Alpay, Y. Ding, Z. L. Wang and C. Brooks, *J. Mater. Chem.*, 2009, **19**, 970-975.
44. L. Yang, S. Luo, Y. Li, Y. Xiao, Q. Kang and Q. Cai, *Environ. Sci. Technol.*, 2010, **44**, 7641-7646.
45. A. Chantre, A. F. J. Levi, R. T. Tung, W. C. Dautremont-Smith and M. Anzlowar, *Phys. Rev. B*, 1986, **34**, 4415-4418.
46. J. P. Bosco, S. B. Demers, G. M. Kimball, N. S. Lewis and H. A. Atwater, *J. Appl. Phys.*, 2012, **112**, 093703.
47. R. Schafranek, J. D. Baniecki, M. Ishii, Y. Kotaka, K. Yamanka and K. Kurihara, *J. Phys. D: Appl. Phys.*, 2012, **45**, 055303.
48. B. Hekmatshoar, D. Shahrjerdi, M. Hopstaken, J. A. Ott and D. K. Sadana, *Appl. Phys. Lett.*, 2012, **101**, 103906.
49. J. Su, L. Guo, N. Bao and C. A. Grimes, *Nano Lett.*, 2011, **11**, 1928-1933.
50. M. T. Mayer, Y. Lin, G. Yuan and D. Wang, *Acc. Chem. Res.*, 2013.
51. V. Sepelak, S. M. Becker, I. Bergmann, S. Indris, M. Scheuermann, A. Feldhoff, C. Kubel, M. Bruns, N. Sturzl, A. S. Ulrich, M. Ghafari, H. Hahn, C. P. Grey, K. D. Becker and P. Heitjans, *J. Mater. Chem.*, 2012, **22**, 3117-3126.
52. C.-X. Zhao, P. Wu, D.-L. Zhang, R. Chen, L.-F. Chi and T. Xiao, *Acta Phys.-Chim. Sin.*, 2010, **26**, 1343-1348.

TOC graphic:

Highly Efficient Visible-Light Driven Photocatalysts: A Case on Zinc Stannate Based Nanocrystal Assemblies

Cai-Hong Liu, Robert Röder, Lichun Zhang, Zheng Ren, Haiyan Chen, Zhonghua Zhang, Carsten Ronning, and Pu-Xian Gao *
* Corresponding author E-mail: puxian.gao@ims.uconn.edu

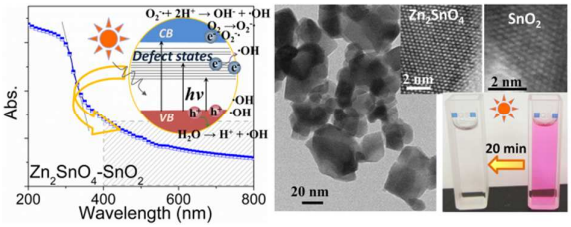

Synopsis: Highly efficient visible-light driven photocatalysts are enabled by wide bandgap semiconducting zinc stannate based nanocrystal assemblies through populating the defect energy states and coherent hetero-interfaces.

Graphic abstract:

Highly Efficient Visible-Light Driven Photocatalysts: A Case on Zinc Stannate Based Nanocrystal Assemblies

Cai-Hong Liu, Robert Röder, Lichun Zhang, Zheng Ren, Haiyan Chen, Zhonghua Zhang, Carsten Ronning, and Pu-Xian Gao *
* Corresponding author E-mail: puxian.gao@ims.uconn.edu

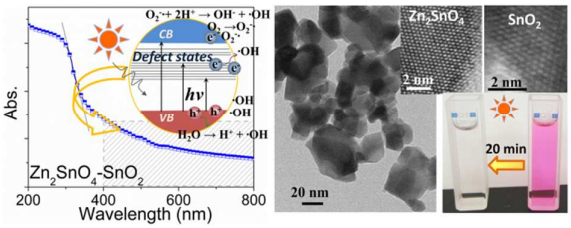

Synopsis: Highly efficient visible-light driven photocatalysts are enabled by wide bandgap semiconducting zinc stannate based nanocrystal assemblies through populating the defect energy states and coherent hetero-interfaces.